



Performance of nano-nickel core wrapped with Pt crystalline thin film for methanol electro-oxidation



Qinbo Yuan, Donghong Duan, Yanhua Ma, Guoqiang Wei, Zhonglin Zhang, Xiaogang Hao, Shibin Liu*

College of Chemistry and Chemical Engineering, Taiyuan University of Technology, Taiyuan 030024, China

HIGHLIGHTS

- Ni@Pt core–shell nanoparticles with Pt nanocrystal thin film are synthesized.
- The Pt shell is small clusters with poorly crystalline of different crystal faces.
- The nanoparticles have considerably higher activity to methanol electro-oxidation.

ARTICLE INFO

Article history:

Received 30 April 2013

Received in revised form

1 July 2013

Accepted 7 July 2013

Available online 16 July 2013

Keywords:

Amorphous

Ni@Pt core–shell

Methanol electro-oxidation

Fourier transform infrared spectroscopy

ABSTRACT

Ni@Pt core–shell nanoparticles with Pt nanocrystal thin film are synthesized by chemical reduction to investigate methanol oxidation. The morphology, structure, and composition of the as-prepared nanoparticles are characterized by aberration-corrected high-resolution transmission electron microscopy, X-ray diffraction, energy dispersive spectroscopy, and X-ray photoelectron spectroscopy. Electrochemical characterizations are performed by cyclic voltammetry, in situ Fourier transform infrared spectroscopy, and chronoamperometry. Results show that the as-prepared nanoparticles have a core–shell nano-structure. Moreover, Pt on the shell is composed of small clusters that are poorly crystalline domains of different crystal faces. The Pt mass activity of the as-prepared nanoparticles is about three times that of conventional E-TEK 40 wt% Pt/C catalysts, and methanol oxidation over the as-prepared nanoparticles is found to occur at a lower overpotential than over Pt/C. The as-prepared nanoparticles also exhibit markedly high resistance to carbon monoxide deactivation. This high electrocatalytic performance can be attributed to the unique structure of the as-prepared nanoparticles.

© 2013 Elsevier B.V. All rights reserved.

1. Introduction

Direct methanol fuel cells (DMFCs) are expected to become a major source of clean energy necessary for transportation because of their rich source, low cost, and high-energy density [1,2]. Despite considerable recent advances, the existing fuel-cell technology still has drawbacks, including the mediocre catalytic activity and instability of Pt electrocatalysts for anodic methanol oxidation reaction (MOR) and cathodic oxygen reduction reaction (ORR) [3]. In particular, methanol electro-oxidation on platinum is a self-poisoning reaction because the stepwise dehydrogenation of methanol produces tenacious CO-like reaction intermediates that cannot be effectively removed at low temperatures. The

accumulation of these intermediates is known to gradually decrease catalytic activity [4].

At present, the catalytic performance of nanocrystals (NCs) can be finely tuned either by their composition to mediate their electronic structure [3,5] or by their shape to determine surface atomic arrangement and coordination [6,7]. Fundamental studies on the {111}, {100}, and {110} index planes or facets typically found on the single-crystal surfaces of bulk Pt reveal that these single-crystal surfaces have much lower activity than high index planes [8,9]. Sun et al. [10] synthesized tetrahedral Pt NCs enclosed by {730} and vicinal high-index facets using a square-wave potential method. The high-index faceted Pt/C catalysts exhibit two to three times higher electrocatalytic activity for ethanol oxidation than commercial Pt/C catalysts. The high index planes have high densities of atomic steps, ledges, and kinks that act as active sites for breaking chemical bonds [8,11]. However, shape-controlled NCs enclosed by high-index facets are challenging to synthesize because of their high surface energy [12].

* Corresponding author. Tel.: +86 351 6111062; fax: +86 351 6018554.
E-mail address: sbliutyut@163.com (S. Liu).

The term heteroepitaxy refers to the ordered growth of crystalline film on a substrate where the overgrowth adopts the symmetry and interatomic spacing of the substrate, thereby forming a strained epitaxial layer. At a critical thickness, transition occurs to match the bulk spacing of the deposited layer, and the strain is relieved by misfit dislocations for example. In the case of an epitaxial metal on metal substrate, the grain size has also been suggested to be largely controlled by the mismatch-dependent lattice strain such that as the film grows, the cumulative strain increases until growth ceases at a certain limiting value. The structure of microcrystalline thin films primarily depends on the mismatch distance, lattice fringes, film thickness, etc. Regarding the structure of microcrystalline films that are less than a few atom layers thick, a large amount of mismatch dislocations, vacancies, and lattice interstitial atoms may exist. The volume of the grain-boundary area is also as large as the total volume of the crystallites in the film. In general, the lattice interstitial atoms randomly occupy the lower energy sites of the crystalline boundaries as a type of crystal. Given the high density of surface defects such as ledges and kinks serving as active sites in high-index planes, microcrystalline films usually exhibit high catalytic activity and stability [13].

Considerable efforts have been devoted to solve the problem of Pt NCs with high-index planes [10]. However, the high cost of Pt is still one of the main disadvantages hindering DMFC commercialization. Core–shell nanostructure may be a reasonable way to decrease Pt loading and enhance the catalytic activity of Pt catalysts because the electrocatalytic process of methanol oxidation occurs at the shell of catalyst nanoparticles [14]. Few attempts on this process have been recently reported. Lim et al. [15] synthesized Pd–Pt bimetallic nanodendrites consisting of a dense array of Pt branches on a Pd core, and these nanodendrites are two and a half times more active for ORR than a state-of-the-art Pt/C catalyst with equivalent Pt mass. Wang et al. [16] used anodized aluminum oxide template-electrodeposition and magnetron sputtering to synthesize a Pd/Pt core–shell nanowire array electrocatalyst whose specific activity for MOR is four times that of conventional E-TEK PtRu/C catalysts. In recent years, Pt@Au/C core–shell catalysts have been investigated and reported by a few groups [17]. However, to the best of our knowledge, few studies have discussed the influence of Pt NC thin films as a shell on methanol electrocatalytic performance. Thus, research on the synthesis and catalytic activities of core–shell Ni@Pt nanoparticles with Pt nanocrystal thin film is valuable.

In this paper, we report the use of Ni as a base coated with Pt NC thin film to form low-cost, high-activity core–shell Ni@Pt nanoparticles. The lattice parameters and bonding characteristics between the two metals, as well as the nucleation and growth of Pt, are affected by differences in crystal forms. The arrangement is mainly in the form of chaotic clusters that result in long- and short-ranged disordered structures. The catalytic performance of Pt nanocluster thin films for methanol oxidation is also studied based on the special characteristics of the metal films. Results show promise toward resolving the mediocre catalytic activity and instability of Pt NCs.

2. Experiment

2.1. Materials

All chemicals used in our experiment were analytical grade. Tetra-*n*-octylammonium bromide (TOAB), lithium triethylborohydride, and tetrahydrofuran (THF) were used as a dispersant, reducing agent, and solvent, respectively. Other reagents include $\text{NiCl}_2 \cdot 6\text{H}_2\text{O}$ ($\geq 98\%$), PtCl_2 ($\geq 99.95\%$), and ethanol ($\geq 99.7\%$).

Deionized water was prepared with a Barnstead Nanopure H_2O purification system (resistance = 18.2 M Ω cm).

2.2. Preparation of core–shell Ni@Pt nanoparticles wrapped with Pt cluster thin film

Core–shell Ni@Pt nanoparticles were prepared as follows. $\text{NiCl}_2 \cdot 6\text{H}_2\text{O}$ (0.0475 g) and TOAB (0.2625 g) were first dissolved in 10 mL of THF. The mixture was completely dissolved after approximately 30 min of ultrasonic dispersion, and then 5.5 mL of lithium triethylborohydride was gradually added. The solution color changed from blue to black, indicating that Ni nanoparticles were obtained. After NiCl_2 was completely reduced (approximately 30 min), a certain amount of PtCl_2 solution was added to the solution and a black suspension was obtained. Ultrasonic stirring was continued for 60 min to complete PtCl_2 reduction. The product was centrifuged at 6000 rpm for 10 min with H-1650. The supernatant was separated, and the precipitate was dispersed in a certain volume of THF, centrifuged at 6000 rpm for 6 min to remove any impurity, and then washed once with THF and thrice with ethanol. After drying in a vacuum oven at 80 °C for 12 h, the precipitate was transferred to a tube furnace and then heated under an argon atmosphere at 400 °C for 1 h.

2.3. Electrode preparation

Ni@Pt/C core–shell electrocatalysts were prepared by dispersing core–shell Ni@Pt nanoparticles on Vulcan XC-72 carbon at 2:3 weight ratio of Ni@Pt:C, and the mixture was ultrasonically dispersed for 10 min. Afterward, 6 μL of the mixture was transferred to a clean glassy carbon electrode (5 mm in diameter) and then immediately dried at 50 °C. Subsequently, 7.2 μL of Nafion was coated on the catalyst followed by drying at 90 °C.

2.4. Physical and electrochemical characterization

The morphology and surface structures of core–shell Ni@Pt nanoparticles were characterized with a D/max-2500 X-ray diffractometer (Cu K α radiation, $\lambda = 0.154056$ nm, scan rates = 8° min $^{-1}$, $2\theta = 5^\circ$ –85°) at 40 kV and 100 mA and with a Titan 80–300 aberration-corrected high-resolution TEM (HRTEM) at 300 W (resolution = 0.08 nm). The elemental composition of the catalysts was determined with an LEO438VP EDX system (USA; electron beam current density = 40 A cm $^{-2}$) operated at 100 kV and with a VG Scientific ESCALab 250i-XL XPS system (Al K α radiation, scanning step = 0.05 eV) operated at 300 V. Spectral correction was based on the graphite C 1s level at 284.6 eV. Overlapping peaks were deconvoluted by the vendor-supplied software XPSPEAK (version 4.1).

Electrochemical characterization was performed on a standard three-electrode cell using an AFMSRXIE-536 rotating disk electrode (PAR Company, USA) connected to a VMP-2 multichannel potentiostat. Pt wire was used as a counter electrode, and Hg|Hg $_2$ SO $_4$ electrode (MSE) was used as a reference electrode. The electrochemical properties of the catalysts were investigated in x M CH $_3$ OH ($x = 0$ and 0.2) and 0.5 M H $_2$ SO $_4$ aqueous solution by CV from -0.65 V to 0.70 V at a sweep rate of y mV s $^{-1}$ ($y = 10$ and 50). An E-TEK 40% Pt/C sample was used for comparison, and the corresponding electrochemical performance was investigated.

In situ Fourier transform infrared (FTIR) spectroscopy studies were performed on a Nicolet 6700 FTIR spectrometer equipped with an MCT/B detector and cooled with liquid nitrogen. The resulting spectrum was calculated as follows [18]:

$$\frac{\Delta R}{R} = \frac{R(E_S) - R(E_R)}{R(E_R)} \quad (1)$$

where $R(E_S)$ and $R(E_R)$ are the single-beam spectra of the reflection collected at the sample potential E_S and the reference potential E_R , respectively. The IR spectral resolution was at 8 cm^{-1} , and 300 interferograms were collected and co-added into each single-beam spectrum, which took approximately 300 s. Measurements were carried out at room temperature unless otherwise indicated.

3. Results and discussion

Fig. 1 shows the XRD patterns of core-shell Ni@Pt nanoparticles with different atomic ratios. The diffraction peaks at 44.3° , 51.7° , and 76.4° can be indexed to the fcc cubic Ni(111), Ni(200), and Ni(220) crystal faces, respectively; those at 39.9° and 46.8° can be indexed to the Pt(111) and Pt(200) crystal faces, respectively. With decreased Pt content, the diffraction peak density of Pt gradually decreases until the atomic ratio of Ni and Pt is >10 , and the diameters of Pt clusters on the Ni cores are so small that the Pt diffraction peak cannot be detected. This finding shows that the Pt atoms on the shell may be present as polycrystalline thin film whose average crystal diameter ranges from approximately 1 nm to 2 nm [19]. By contrast, when the atomic ratio of Ni and Pt is <5 , the Pt diffraction peak can be detected, which shows that the Pt atoms on the shell have large crystals. Given that the strength of the electronic inductive effect of Ni on Pt NCs gradually increases with decreased shell thickness, the lattice parameter of Ni expands and the diffraction peak of Ni exhibits a slight negative shift. This finding indicates that the strong interfacial tension is transformed from the dislocation energy of the atoms between Pt NCs. The lattice parameter of Ni is $a = 0.3529 \text{ nm}$ and that of Pt is $a = 0.3923 \text{ nm}$. The dislocation value (Δa) is 0.0394 nm , which is approximately 11.2% of a ($\Delta a/a > 5\%$). This value induces the dislocation of the Pt crystal plane with that of the Ni core during crystal nucleus formation and Pt crystal growth. Moreover, numerous Pt NCs and interfacial atoms are found between them, and the number is considerably large such that the interfacial volume occupied by the interfacial atoms is close to that of the Pt crystals.

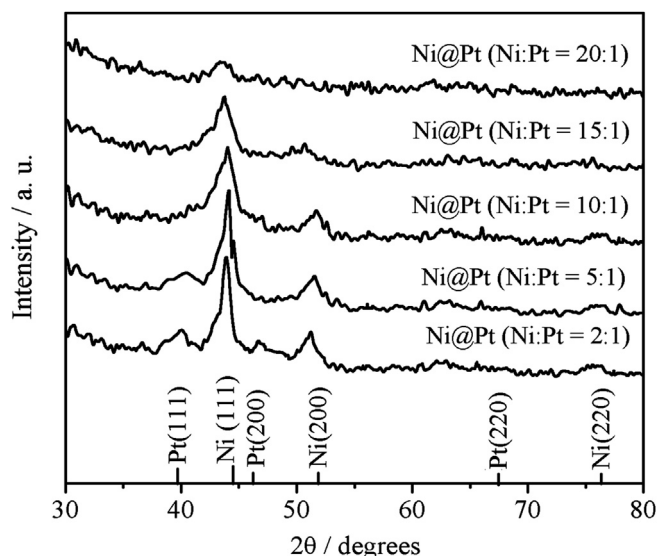


Fig. 1. Powder XRD patterns of the core-shell Ni@Pt nanoparticles at different Ni/Pt atomic ratios: Ni:Pt = 2:1, Ni:Pt = 5:1, Ni:Pt = 10:1, Ni:Pt = 15:1, and Ni:Pt = 20:1.

The morphology of the core-shell Ni@Pt (Ni:Pt = 15:1) nanoparticles is investigated by aberration-corrected high-resolution TEM. The corresponding images are presented in Fig. 2. Fig. 2a shows that the diameter of the nanoparticles is approximately 12 nm. Fig. 2b shows that the as-prepared nanoparticles have a core-shell structure and an average diameter of approximately 12 nm. The average thickness of the Pt layer on the surface of the Ni nanoparticles is approximately 2 nm. Fig. 2c and d shows the particle surface harboring many nanoscale crystals with different lattice planes. The observed lattice fringes well fit the Pt(111), {100}, and even {110} surfaces. Furthermore, many interfacial atoms that usually serve as active sites for breaking chemical bonds, such as atomic steps, ledges, and kinks in high-index planes, are found between the crystals. The atomic ratios of Ni:Pt in Ni@Pt (Ni:Pt = 15:1) nanoparticles determined by EDX are 15.67:1, consistent with the molar ratio in the starting precursor salts. For comparison, the surface Ni:Pt atomic ratios in the Ni@Pt (Ni:Pt = 15:1) nanoparticles determined by XPS are 10.59:1. These results indicate that the atomic content Ni/Pt ratios are remarkably lower than the corresponding bulk atomic content Ni/Pt ratios measured by EDX, which can be ascribed to the photoelectron attenuation lengths ranging from approximately 2 nm to 5 nm. This result further confirms that the outer Pt-rich shell coats the inter Ni core.

Fig. 3 shows the XPS responses of the prepared core-shell Ni@Pt nanoparticles in the Ni 2p and Pt 4f regions. The binding energy (BE) scale is calibrated by measuring the C 1s peak (BE = 284.6 eV). In the Ni 2p region, the peak positions at 852.3 and 869.7 eV for Ni 2p_{3/2} and Ni 2p_{1/2} may be assigned to metallic nickel, respectively. The characteristic peaks at around 855, and 861 eV correspond to Ni²⁺ in the NiO species [20]. This result shows that the cores of the nanoparticles are present as Ni and NiO. In the Pt 4f region, overlapping peaks are deconvoluted by the Gauss-Lorentzian fitting method, and the peaks are identified as different oxidation states. The peaks at around 71 and 74 eV can be assigned to Pt 4f_{7/2} and Pt 4f_{5/2} of metallic platinum, respectively. The peaks at higher BE correspond to Pt²⁺ in PtO/Pt(OH)₂ (72 and 75 eV) species in the composites. Pt is predominantly present as metallic Pt along with surface oxides, as commonly observed in the case of ultrafine Pt particles [21]. The Pt 4f_{7/2} BE corresponds to metallic Pt for Ni@Pt nanoparticles with Ni:Pt 2:1, 5:1, 10:1, 15:1, and 20:1 located at 71.30, 71.25, 71.17, 71.08, and 71.05 eV, respectively. Pt in the Ni@Pt nanoparticles has lower BE values than bulk Pt (71.49 eV) [22], similar to previous findings [23]. The downshift of the Pt BE can be attributed to the effect of Ni cores. Moreover, Pt BE decreases with decreased Pt contents. Larger Ni/Pt atomic ratios result in lower Pt BE values, indicating that the electronic structure of Pt is modified upon deposition onto the surface of Ni nanoparticles. The electronic effect between Pt and Ni increases with decreased Pt content in the Ni@Pt nanoparticles.

We hypothesize that the Ni cores exert an electronic effect on the shell that is in direct contact with the substrate and that the cores exhibit the same effect as Ni cores with the same diameter. Hence, the Pt polycrystalline thin film exhibits a more powerful electronic induction effect with increased Ni:Pt atomic ratio. Ni atom has fewer bonding *d* electrons than Pt atom. Given that the Pt shell is built on Ni cores, some bonding *d* electrons in the Pt NCs of the shell shift to the *d* electron band of the Ni cores. Meanwhile, some *s* electrons of the Ni core shift to the *s* electron band of Pt NCs; thus, the Pt shell acquires more electrons than the Ni core and carries a negative charge because the electronegativity of Pt is higher than that of Ni. However, when the atomic ratio of Ni:Pt is $>15:1$, the number of NCs in the shell increases and the diameter decreases to only several atoms. In addition, numerous interfacial atoms acquire very high interfacial energy between the Pt NCs.

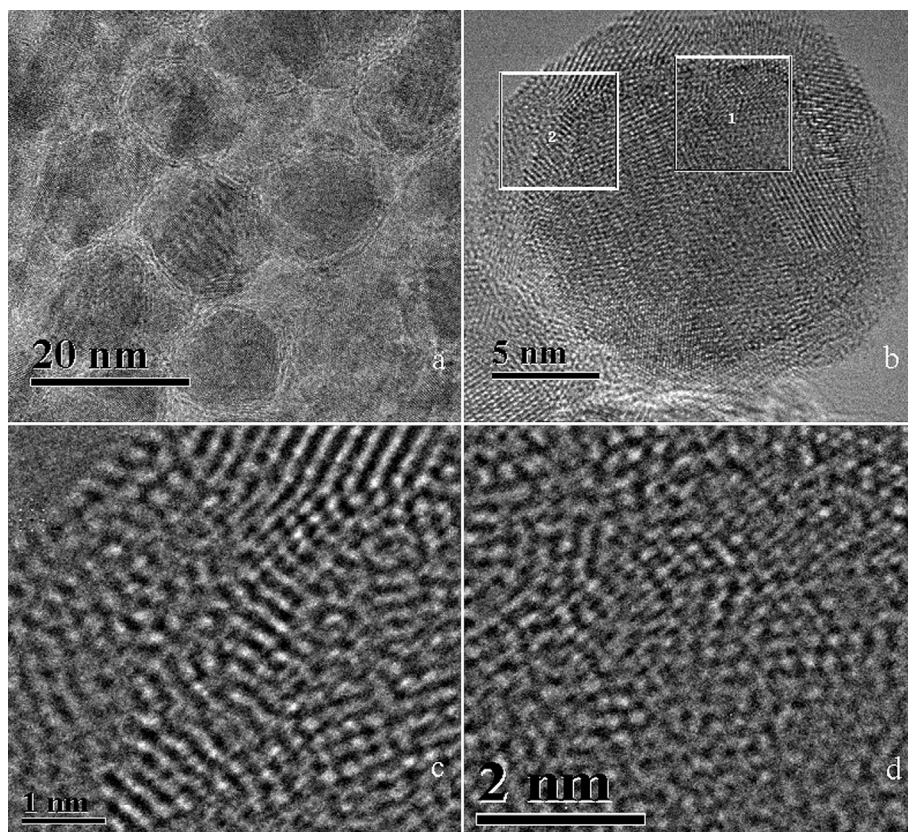


Fig. 2. Aberration-corrected high-resolution TEM images of unsupported core-shell Ni@Pt (Ni:Pt = 15:1) nanoparticles.

Generally, high interfacial energy atoms are very active when they are in the oxidation state such as PtO or PtOH under the condition of oxygen adsorption potential [3].

The electrocatalytic activities toward the ORR of the as-synthesized core-shell Ni@Pt catalysts and commercial Pt/C catalysts are evaluated by cyclic voltammetry (CV) in 0.5 M H₂SO₄ solution. Fig. 4 shows that the current density of oxygen adsorption and desorption on the core-shell Ni@Pt catalysts is larger than that on Pt/C catalysts within the potential range of 0.0 V–0.7 V. The

charge density of oxygen adsorption on the core-shell Ni@Pt catalysts is 2272 mC mg^{−1} Pt, whereas that on the Pt/C catalysts is only 632 mC mg^{−1} Pt. These CV data also confirm that the core-shell Ni@Pt catalysts have higher density of active sites on their surface than Pt/C catalysts. The corresponding voltage to the peak current density of oxygen species on the as-prepared catalysts positively shifts compared with Pt/C catalysts, illustrating that the adsorption energy of the oxygen species on catalysts weakens with increased Pt content.

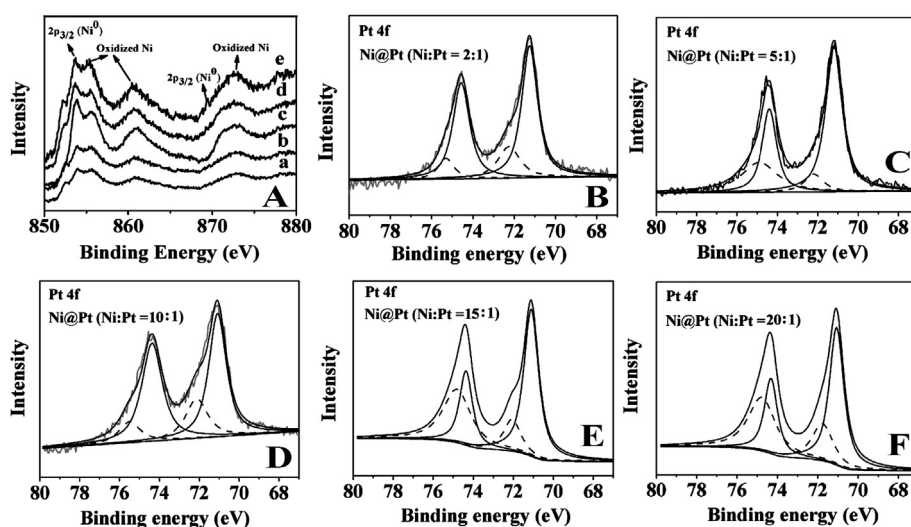


Fig. 3. XPS spectra for core-shell Ni@Pt nanoparticles: (A) Ni 2p peaks of the Ni@Pt nanoparticles at different Ni/Pt atomic ratios: (a) Ni:Pt = 2:1, (b) Ni:Pt = 5:1, (c) Ni:Pt = 10:1, (d) Ni:Pt = 15:1, and (e) Ni:Pt = 20:1. (B–F) Pt 4f peaks of the Ni@Pt nanoparticles, overlapping peaks are deconvoluted, and the peaks are identified as different oxidation states.

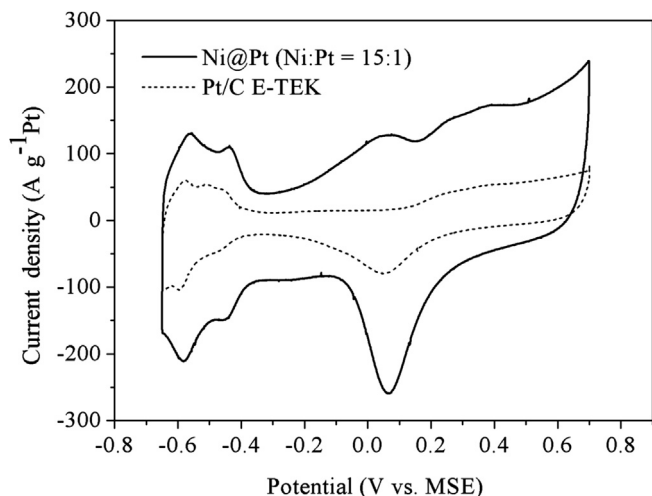


Fig. 4. Cyclic voltammograms for the core-shell Ni@Pt (Ni:Pt = 15:1) nanoparticles and Pt/C catalysts at room temperature in N_2 -saturated 0.5 M H_2SO_4 solutions at a scan rate of 50 mV s^{-1} .

The activity of a catalyst is controlled by catalytic and geometrical properties. Thus, the electrochemically active surface area (EAS) of the catalysts is one of the most important parameters for determining electrocatalytic activity for methanol oxidation, which occurs on the surface of Pt particles [24]. The EAS of the different catalysts is calculated using Eq. (2):

$$A_{EL} = \frac{Q_H}{k \times m_{Pt}} \quad (2)$$

where Q_H is the integral of the hydrogen desorption peak on the Pt surface ($C \text{ m}^{-2}$), k is the charge required to oxidize a monolayer of hydrogen on the Pt surface ($\sim 2.1 \text{ C m}^{-2}$), and m_{Pt} is Pt loading on the glassy carbon electrode (g m^{-2}) [25]. The results are 196.24 and $34.96 \text{ m}^2 \text{ g}^{-1} \text{ Pt}$ for Ni@Pt (Ni:Pt = 15:1) and Pt/C catalysts, respectively. A significant difference is observed in the EAS values, and the EAS of H_2 desorption peaks are larger for Ni@Pt catalysts than for Pt/C catalyst, indicating better Pt utilization of core-shell nanostructure catalysts than Pt/C catalyst. The hydrogen adsorption/desorption regions exhibit the presence of various facets on the surfaces of Pt particles, such as {110}, {111}, and {100} planes, as well as the effects of edges, corners, and terraces [26,27].

Fig. 5 compares the cyclic voltammograms of Ni@Pt catalysts and commercial Pt/C catalysts recorded in 0.2 M CH_3OH and 0.5 M H_2SO_4 . In the potential scan in the positive and negative directions, the current density measured on the Ni@Pt catalysts is up to 2.9 times as high as that of Pt/C catalysts in the forward scan. The adsorbed residue of methanol (e.g., $Pt-CO$) is difficult to oxidize at low potentials; thus, it constitutes a catalytic poison. Moreover, methanol oxidation over the as-prepared nanoparticles is found to occur at a lower overpotential (-0.24 V) than over Pt/C (-0.20 V). The low ratio of the forward anodic peak current density (I_f) to the reverse anodic peak current density (I_b) is used to describe the high tolerance of the catalysts on the accumulation of carbonaceous species [3]. Fig. 5 shows that the ratio for Pt/C is 1.06 and that for Ni@Pt is 1.57. The low I_f/I_b ratio for the Pt/C catalysts indicates poor oxidation of methanol to carbon dioxide during the anodic scan, and a large amount of intermediate carbonaceous substances is trapped on the catalyst surface in the forward scan. This finding suggests that the as-prepared Ni@Pt catalysts have stronger tolerance to intermediate carbonaceous substances than Pt/C catalysts. The factors that improve activity include the disordered arrangement of some surface atoms of Pt NC thin film, leading to numerous

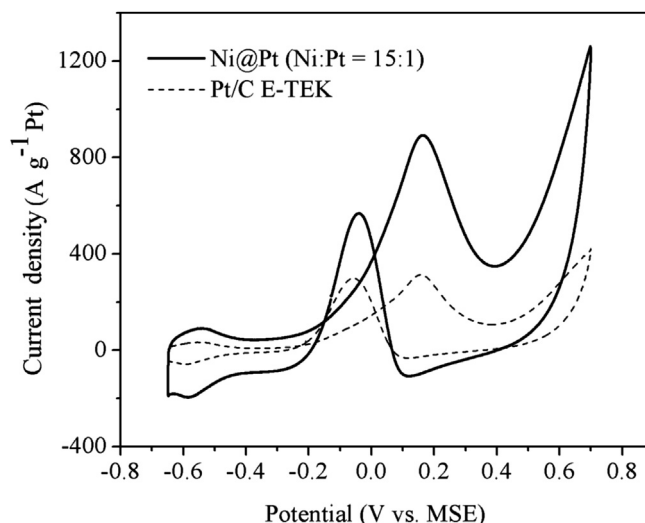


Fig. 5. Cyclic voltammograms for the core-shell Ni@Pt (Ni:Pt = 15:1) nanoparticles and Pt/C catalysts at room temperature in N_2 -saturated 0.2 M CH_3OH + 0.5 M H_2SO_4 solutions at a scan rate of 10 mV s^{-1} .

highly unsaturated coordination atoms on the surface with very strong surface energy and activation energy [19], thereby easily reacting with the reactants.

Chronoamperometric experiments are carried out to evaluate the long-term performance of the catalysts toward MOR under continuous operating conditions [28]. Fig. 6 shows plots of current versus time recorded at 0.2 V for 5200 s. At short testing times, the oxidation current rapidly decays for all catalysts possibly because of catalyst poisoning by intermediate species, such as CO_{ads} , CH_3O-H_{ads} , CHO_{ads} , and OH_{ads} , which form during MOR [29]. After 3000 s, the rate of current decay gradually slows and remains pseudo-stable. The current density of Ni@Pt catalysts is approximately 2.5 times higher than that of Pt/C catalysts at 5200 s, demonstrating that the electrocatalytic stability of the Ni@Pt catalysts for methanol oxidation is higher than that of Pt/C catalysts.

Fig. 7 illustrates the in situ FTIR spectra of methanol oxidation on Ni@Pt and Pt/C catalysts at 0.7 V. A small downward band is

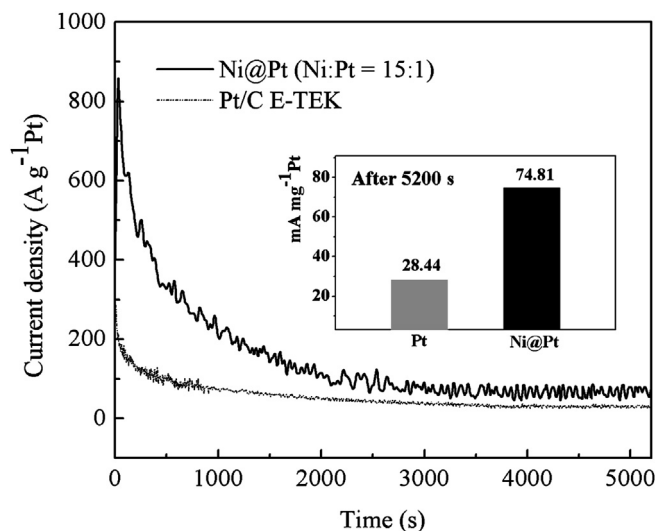


Fig. 6. Chronoamperometric curves of N_2 -saturated 0.2 M CH_3OH + 0.5 M H_2SO_4 solutions at Ni@Pt (Ni:Pt = 15:1) and Pt/C catalyst electrodes for 5200 s. Fixed potential: 0.2 V.

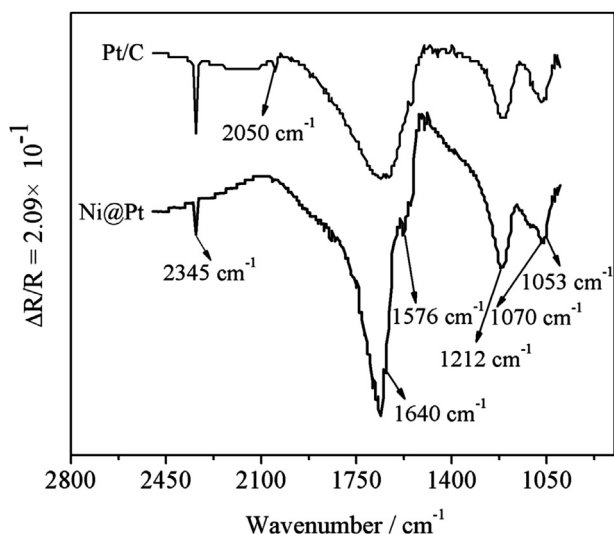


Fig. 7. In situ FTIR spectra for methanol oxidation on Ni@Pt (Ni:Pt = 15:1) and Pt/C catalysts at 0.7 V in N_2 -saturated 0.2 M CH_3OH + 0.5 M H_2SO_4 solutions, reference spectra collected at -0.15 V, and the resolution is 8 cm^{-1} .

observed near 2050 cm^{-1} , which can be attributed to CO_L . The downward bands at 1576 and 1212 cm^{-1} are ascribed to the symmetric stretching vibration frequencies of C–O–C in methylformate. The negative approaching direction of the band at 1640 cm^{-1} can be assigned to $\sigma_{C=O}$ in formaldehyde. The band at 1053 cm^{-1} can be assigned to HSO_4^- in the solution. More methylformate and fewer CO are clearly formed on Ni@Pt catalysts than on Pt/C catalysts. Consequently, the Ni@Pt catalysts show higher selectivity for the complete oxidation of methanol to CO_2 .

The aforementioned data further confirm that the as-prepared catalysts show higher tolerance to CO and catalytic activity than Pt/C catalysts. The improved activity effect of the Ni cores and interfacial atoms toward methanol electro-oxidation may have additional applications in fuel cells. The author holds that the reasons below can explain the aforementioned phenomenon. Nørskov et al. [30,31] have recently proposed a model describing the activity of metal adlayers whose characteristics of surface metal d bands particularly the weighted center (ϵ_d) is crucial to the determination of surface reactivity. Density functional theory (DFT) calculations show that the binding energies and reactivity of small adsorbates correlate well with the position of d on metal overlayers [32]. Roudgar et al. [33] used DFT calculations to demonstrate significant coupling of d orbitals of small Pd clusters to Au(111) substrate. An equivalent type of interaction between Pt and Ni can account for the observed activity of Pt. Meanwhile, Pt atoms with low coordination numbers have higher-lying d states, which are more reactive and interact more strongly with the adsorbate states [34]. The platinum NC thin film on the Ni cores has a high degree of defects, high concentration of coordinate unsaturated sites and abounds, and high surface energy, thereby exhibiting high activation energy for the oxidation of CO intermediates and activating molecular H_2O at room temperature [35–37]. According to the mechanism of methanol electro-oxidation on the Pt surface, the decrease in the adsorption energy of CO and the enhancement in the activation of H_2O molecules can considerably improve the activity of Pt nanoparticles.

4. Conclusion

The core–shell Ni@Pt nanoparticles are synthesized by sequential chemical reduction with the aid of surfactants. XRD, EDS,

XPS, and HRTEM confirm the core–shell nanostructure with Pt NC thin film on the shell. The electrochemical performance of the core–shell Ni@Pt catalysts for methanol oxidation is evaluated by CV. Results show that the catalysts exhibit considerably enhanced activity toward methanol electro-oxidation compared with commercial E-TEK 40% Pt/C catalysts. In situ FTIR of the methanol oxidation demonstrate that the catalysts have high CO tolerance. These findings raise promising possibilities for synthesizing improved methanol electro-oxidation Pt-based catalysts, as well as for stabilizing Pt and other Pt-group metals, under the anodic conditions of DMFCs.

Acknowledgment

The authors acknowledge the support of research project NSFC (20676088) provided by China National Natural Science Foundation.

References

- [1] H.A. Gasteiger, S.S. Kocha, B. Sompalli, F.T. Wagner, *Appl. Catal. B Environ.* 56 (2005) 9–35.
- [2] P.J. Ferreira, G.J. la O', Y. Shao-Horn, D. Morgan, R. Makharia, S. Kocha, H.A. Gasteiger, *J. Electrochem. Soc.* 152 (2005) A2256–A2271.
- [3] J. Zhang, K. Sasaki, E. Sutter, R.R. Adzic, *Science* 315 (2007) 220–222.
- [4] E.A. Batista, G.R.P. Malpass, A.J. Motheo, T. Iwasita, *J. Electroanal. Chem.* 571 (2004) 273–282.
- [5] V.R. Stamenkovic, B. Fowler, B.S. Mun, G.F. Wang, P.N. Ross, C.A. Lucas, N.M. Markovic, *Science* 315 (2007) 493–497.
- [6] R. Narayanan, M.A. El-Sayed, *Nano Lett.* 4 (2004) 1343–1348.
- [7] F.J. Vidal-Iglesias, F.J. Solla-Gullón, J. Rodríguez, P. Herrero, E. Montiel, V. Feliu, J.M. Aldaz, *Electrochem. Commun.* 6 (2004) 1080–1084.
- [8] S. Sun, A. Chen, T. Huang, J. Li, Z. Tian, *J. Electroanal. Chem.* 340 (1992) 213–226.
- [9] N. Tian, Z. Zhou, S. Sun, *Chem. Commun.* 0 (2009) 1502–1504.
- [10] Z. Zhou, Z. Huang, D. Chen, Q. Wang, N. Tian, S. Sun, *Angew. Chem. Int. Ed.* 49 (2010) 411–414.
- [11] G.A. Somorjai, D.W. Blakely, *Nature* 258 (1975) 580–583.
- [12] H.E. Buckley, *Crystal Growth*, Wiley, New York, 1951, pp. 30–385.
- [13] N. Tian, Z.Y. Zhou, S.G. Sun, Y. Ding, Z.L. Wang, *Science* 316 (2007) 732–735.
- [14] J. Luo, L. Wang, D. Mott, P.N. Njoki, Y. Lin, T. He, Z. Xu, B.N. Wanjana, I.L.S. Lim, C. Zhong, *Adv. Mater.* 20 (2008) 4342–4347.
- [15] B.K. Lim, M.J. Jiang, P.H.C. Camargo, E.C. Cho, J. Tao, X.M. Lu, Y.M. Zhu, Y.N. Xia, *Science* 324 (2009) 1302–1305.
- [16] H. Wang, C. Xu, F. Cheng, M. Zhang, S. Wang, S.P. Jiang, *Electrochem. Commun.* 10 (2008) 1575–1578.
- [17] N. Kristian, X. Wang, *Electrochem. Commun.* 10 (2008) 12–15.
- [18] S.G. Sun, Y. Lin, *Electrochim. Acta* 41 (1996) 693–700.
- [19] G. Wang, H. Wu, D. Wexler, H. Liu, O. Savadogo, *J. Alloys Compd.* 505 (2010) L1–L4.
- [20] Y. Zhao, X. Yang, J. Tian, F. Wang, L. Zhan, *Int. J. Hydrogen Energy* 35 (2010) 3249–3257.
- [21] E.A. Anumol, P. Kundu, P.A. Deshpande, G. Madras, N. Ravishankar, *ACS Nano* 5 (2011) 8049–8061.
- [22] Y. Chen, Z. Liang, F. Yang, Y. Liu, S. Chen, *J. Phys. Chem. C* 115 (2011) 24073–24079.
- [23] X. Fu, Y. Liang, S. Chen, J. Lin, D. Liao, *Catal. Commun.* 10 (2009) 1893–1897.
- [24] H. Tong, H. Li, X. Zhang, *Carbon* 45 (2007) 2424–2432.
- [25] B. Lim, X. Lu, M. Jiang, P.H.C. Camargo, E.C. Cho, E.P. Lee, Y. Xia, *Nano Lett.* 8 (2008) 4043–4047.
- [26] A. Chen, P. HolteHindle, *Chem. Rev.* 110 (2010) 767–804.
- [27] C. Bianchini, P.K. Shen, *Chem. Rev.* 109 (2009) 183–206.
- [28] R. Chetty, W. Xia, S. Kundu, M. Bron, T. Reinecke, W. Schuhmann, *Langmuir* 25 (2009) 3853–3860.
- [29] A. Kabbabi, R. Faure, R. Durand, B. Beden, F. Hahn, J.M. Leger, C. Lamy, *J. Electroanal. Chem.* 444 (1998) 41–53.
- [30] J. Greeley, J.K. Nørskov, M. Mavrikakis, *Annu. Rev. Phys. Chem.* 53 (2002) 319–348.
- [31] B. Hammer, J.K. Nørskov, *Advances in Catalysis* 45, Elsevier, Amsterdam, 2000, pp. 71–129.
- [32] Y. Xu, A.V. Ruban, M. Mavrikakis, *J. Am. Chem. Soc.* 126 (2004) 4717–4725.
- [33] A. Roudgar, A. Groß, *Surf. Sci.* 559 (2004) L180–L186.
- [34] N. Lopez, J.K. Nørskov, *J. Am. Chem. Soc.* 124 (2002) 11262–11263.
- [35] Y.D. Kim, M. Fischer, D. Stolcic, M. Fischer, G. Ganteför, Y.D. Kim, Q. Sun, P. Jena, *Chem. Phys. Lett.* 377 (2003) 170–176.
- [36] D. Stolcic, M. Fischer, G. Ganteför, Y.D. Kim, Q. Sun, P. Jena, *J. Am. Chem. Soc.* 125 (2003) 2848–2849.
- [37] B.E. Salisbury, W.T. Wallace, R.L. Whetten, *Chem. Phys.* 262 (2000) 131–141.